V European Conference on Computational Fluid Dynamics
ECCOMAS CFD 2010
J. C. F. Pereira and A. Sequeira (Eds)
Lisbon, Portugal, 14–17 June 2010

MULTI-SCALE FEATURES OF BAROCLINIC WAVES IN SOUND-PROOF, GLOBAL SIMULATIONS WITH EULAG (ECCOMAS CFD 2010)

Joseph M. Prusa[*] and William J. Gutowski[†]

[*]Teraflux Corporation
Boca Raton, FL USA
e-mail: jprusa@bellsouth.net

[††]Iowa State University
Ames, IA 50011
gutowski@iastate.edu

Key words: Fluid Dynamics, anelastic, baroclinic instability, gravity waves, global model.

Abstract. *EULAG is a computational model for simulating flows across a wide range of scales and physical scenarios [1]. It is noteworthy for its grid adaptive technology, nonoscillatory forward-in-time integration, robust Krylov solver, and parallel scalability. The standard option for EULAG employs an anelastic approximation to capture nonhydrostatic effects and simultaneously filter sound sound waves from the solution. Early global applications of EULAG demonstrated that it is capable of closely matching previously published idealized Held-Suarez climates [2]. A more recent application of EULAG to aqua-planet simulations has demonstrated its potential as a dynamics core with grid adaptive capabilities for climate models [3,4].*

In this paper, we examine the breaking of planetary waves and the resulting generation/ radiation of gravity wave packets in idealized Held-Suarez climates [5]. Using 1.4^o horizontal resolution, EULAG simulations show the generation of pure internal waves from frontal collapse. These waves are small enough that coriolis effects are negligible. Measurable nonhydrostatic effects are also observed, but they are small. EULAG simulations for the baroclinic instability test of Jablonowski and Williamson [6] are also presented. EULAG solutions yield growth rates and disturbance amplitudes similar to [6] for a seeded perturbation, as well as extremely similar phase speeds during the linear growth regime of the nascent baroclinic instability. After ~ 8 days, vigorous baroclinic wavebreaking commences, at which point EULAG results begin to depart in some details from the hydrostatic results shown in [6]. General agreement in the global structure of the solution remains.

1 INTRODUCTION

EULAG is a computational model with options to solve transport equations using either EUlerian (flux form) or LAGrangian (advective form) numerics, hence it's name. Other noteworthy features of EULAG are its NFT (Nonoscillatory Forward-in-Time) integration, robust preconditioned non-symmetric Krylov solver for pressure, proven scalability on massively parallel architectures, dynamic grid adaptivity enabled by continous remappings of coordinates, and nonhydrostatic dynamics [1].

EULAG has a proven record of successful application to turbulent flows, and has options for DNS (Direct Numerical Simulation), LES (Large Eddy Simulation), and a default of ILES (Implicit Large Eddy Simulation). Other successful applications have been made in urban flows, gravity wave dynamics, flows past complex/moving boundaries, micrometeorology, cloud microphysics and dynamics, global atmospheric circulation, and basic fluid dynamics of incompressible fluids. Derivatives of EULAG have also been applied to simulations of visco-elastic waves in the human brain, oceanic flows, and stellar convection (see [1] for references). The distinctness of MPDATA's ILES methodology compared to other high-resolution schemes is emphasized in [7, 8]. In these studies, the authors provide a framework for how MPDATA ILES can produce LES without invoking explicit SGS (SubGrid-Scale) models.

The default analytic formulation of EULAG assumes the nonhydrostatic *anelastic* equations of motion. The anelastic approximation is an example of a filtering process to make equations that are *sound–proof*, that is, CFL stability of explicit integration is not affected by the speed of sound. Other well known examples of filtered, sound–proof approximations are the hydrostatic and Bousinesq approximations. In the hydrostatic approximation, the assumption is made that local departures from a hydrostatic, albeit stratified fluid, are negligible (→ very small vertical wind). In the Boussinesq approximation, the assumption is made that density variation is negligibly small (density ~ constant) and affects only the buoyancy term. In the anelastic approximation, both nonhydrostatic physics and stratified ambient states are retained. Instead, the assumptions are that (i) the vertical scale of motion is much smaller than the local potential temperature scale height, and (ii) perturbations of the dependent fields from a basic state are small enough that terms that are quadratic in perturbations are negligible [9]. The basic state is an ambient state in hydrostatic equilibrium. The anelastic assumptions allow the linearization of pressure gradient forces and mass fluxes in the momentum and mass conservation equations, respectively – numerical approximations that greatly facilitate the design of second-order accurate, flexible NFT models that are implicit with respect to inertia-gravity waves [10].

As documented in the literature, the anelastic approximation is known to be accurate for atmospheric modelling up to synoptic scales [11]; is used successfully in astrophysics for modeling solar and stellar convection zones [12, 13]; and has led to simulations that successfully explain the superrotation of the Earth's solid inner core [14, 15]. For research studies of multi-scale geophysical fluids, we have also found the anelastic approximation to be beneficial. However, the suitability of this approximation for global atmospheric applications has often been criticized. Arguments against the anelastic model using normal mode analysis have been given in [16]. There it is found that the anelastic model distorts the phases of deep planetary wave modes, a result that is not inconsistent with assumption (i) above.

Within the framework of EULAG, the anelastic model readily generalizes into either a compressible/incompressible Boussinesq, or incompressible Euler system [2]. Recent work has focused on developing options for fully compressible equations for high-speed

flows [17], Durran's pseudo-incompressible system [18], and fully compressible equations for low and moderate Mach number flows. The Durran equations are of special interest because they conveniently separate baroclinicity *per se* from compressibility effects, thus enabling inquiries into the role of baroclinicity in fluid states close to bifurcation. The role of compressibility versus baroclinicity is of particular interest in weather and climate prediction and lies at the heart of the anelastic controversy. The modal analysis [16] predicts Durran's approximation will have no phase error; whereas the EULAG variant using Durran's approximation shows negligible differences from the default anelastic solution [18] for deep modes. A recent multiple parameter, singular perturbation study [19] using the method of distinguished limits finds that anelastic models gets the multiscale interaction between local gravity waves and synoptic scale planetary waves *asymptotically close*. This means that all differences between elastic and anelastic models are of order $O(M^{2/3})$ or smaller, where M is the Mach number. This translates into allowable stratifications of ~10% of the local mean potential temperature over a pressure scale height of the atmosphere.

The motivation for the present study is twofold. First, in Section 3 we examine in some detail the generation of a localized gravity wave packet due to frontal collapse in Held-Suarez simulations. The success of EULAG in revealing such waves with modest resolution may be due, in part, to the asymptotically correct scale interaction revealed in [19], as well as to the numerical qualities of the model described in Section 2.3, below. Second, in Section 4 we compare EULAG simulations of the idealized baroclinic instability test to those presented in [5]. Results show extremely good quantitative agreement in phase speeds during the linear growth regime. Once planetary wavebreaking commences, notable differences in some details appear, although other details remain reasonably close and overall general agreement is seen.

2 COMPUTATIONAL MODEL

The model equations presented here are only for the dynamical variables; the interested reader is referred to [20 and 3, 1] and the references therein for generalizations involving moisture and chemistry. The nature of physical forces other than buoyancy, pressure, and Coriolis is explicitly unspecified. Because the grid adaptivity technology of EULAG is based upon coordinate transformations, a tensorial form of the model equations lies at the heart of the model. For clarity, a concise symbolic operator-form description of the governing equations is shown below; for details of the orginal tensorial exposition – required for coding as well as diagnostics – refer to [21] and later references given in [1].

2.1 Salient Analytical Details

The problem to be solved by EULAG is posed in a physical space $\mathbf{S_p}$, with coordinates (t, x, y, z). The governing equations for this space may be any stationary, orthogonal system of coordinates (e.g, Cartesian, cylindrical, spherical). Other systems (e.g., toroidal, …) can also be accomodated in principle, but require coding of the relevant metric coefficients. Appropriate choices for particular coordinate systems are based upon the physics under investigation as well as the geometry of the problem. EULAG transforms the physical representation of the problem and solves it in a computational space $\mathbf{S_t}$ with coordinates $(\bar{t}, \bar{x}, \bar{y}, \bar{z})$. In this transformed space, the grid is always uniform and stationary. Details may be found in [21, 22, 10, 23, 1].

In the generalized coordinates of $\mathbf{S_t}$ the anelastic equations of Lipps & Hemler [9] take on the form:

$$\overline{\nabla} \bullet (\rho^* \overline{v}^s) = 0 \tag{1}$$

$$\frac{d\mathbf{v}}{d\bar{t}} = -\tilde{\mathbf{G}}(\overline{\nabla}\pi') - \mathbf{g}\frac{\theta'}{\theta_o} - \mathbf{f} \times \mathbf{v}' + \mathbf{M}' + \mathbf{D} \tag{2}$$

$$\frac{d\theta'}{d\bar{t}} = -\overline{\mathbf{v}}^s \bullet \overline{\nabla}\theta_e + H \tag{3}$$

Here **v** is the physical velocity; θ, ρ, and π denote the potential temperature, density, and density normalized pressure; **g** and **f** are gravitational and coriolis accelerations; and **D** and H denote viscous dissipation of momentum and heat, respectively. Primes denote deviations from Coriolis-balanced hydrostatic environmental states, denoted with subscript "e". Subscript "o" denotes the basic state, a horizontally homogeneous, con-stant stability hydrostatic reference state used in the anelastic approximation. $\rho^* \equiv \rho\overline{G}$ where $\overline{G}$ is the Jacobian of the coordinates describing $\mathbf{S_t}$ and $\rho = \rho_o$ is understood.

The coordinate system used to describe $\mathbf{S_p}$ generally has some metric structure compared to Cartesian. In the case at hand – spherical coordinates – there are geospherical terms that contribute to **M** in the momentum equations. Additionally, the metric structure of non Cartesian orthogonal systems contribute to the renormalized Jacobi matrix $\tilde{\mathbf{G}}$ (i.e., it is not a Kronecker delta), as well as in numerous transformations made throughout the model. It is also worth noting that two other forms of velocity enter into the model, the *solenoidal* velocity $\overline{\mathbf{v}}^s$ (in continuity and potential temperature), and the *contravariant* velocity $\overline{\mathbf{v}}^*$ that lies inside the advective operator $d/d\bar{t} = \partial/\partial\bar{t} + \overline{\mathbf{v}}^* \bullet \overline{\nabla}$ in Eqs. (2,3). Use of multiple forms of the velocity minimizes the generation of Christoffel symbols (transformation terms that account for the bending and twisting of coordinates) and help to improve accuracy (via the rigorous implementation of tensor identities throughout the model). In the more general case of grid adaptation, these identities allow uniform second order accuracy to be maintained.

2.2 Salient Numerical Details

Each prognostic equation (2,3) of the anelastic system can be written in two equivalent forms, either a Lagrangian or Eulerian evolution equation. Since the Eulerian option is used exclusively in this study, we present only the Eulerian conservation form:

$$\frac{\partial \rho^* \psi}{\partial \bar{t}} + \overline{\nabla} \bullet (\rho^* \overline{\mathbf{v}}^* \psi) = \rho^* R \tag{4}$$

Here ψ symbolizes the components of **v** or θ', and R denotes the associated RHS.

The conservation form (4) as well as the analogous semi-Lagrangian form are approximated to second order accuracy in time and space using an NFT (nonoscillatory forward-in-time) algorithm – see [24] for a review. The default NFT algorithms utilized in EULAG can be formally written in the form:

$$\psi_i^{n+1} = LE_i(\tilde{\psi}) + 0.5\Delta\bar{t}\, R_i^{n+1} \equiv \hat{\psi}_i + 0.5\Delta\bar{t}\, R_i^{n+1} \tag{5}$$

where ψ_i^{n+1} is the solution sought at the grid point $(\bar{t}^{n+1}, \overline{\mathbf{x}}_i)$; $\tilde{\psi} \equiv \psi^n + 0.5\Delta\bar{t}\, R_i^n$; and LE denotes a two-time-level NFT transport operator (e.g., MPDATA for the Eulerian option [25]).

For the current problem (inviscid adiabatic dynamics), the numerical equation (5) represents a system implicit with respect to all dependent variables in (2) and (3). Ultimately it leads to a system that is inverted algebraically to construct expressions for the solenoidal velocity components which are then substituted into the continuity Eq. (1) producing an elliptic equation for the pressure perturbation π'. Details of this projection are given in the appendix of [21]. The elliptic problem with appropriate boundary conditions is solved via a preconditioned, generalized conjugate residual solver (a type of nonsymmetric Krylov solver, [26]). Given the updated pressure perturbation and solenoidal velocities, the updated physical and contravariant velocities may be computed using straightforward tensor transformations (see [21]). Exact conservation for mass can, in principle, be made to the level of round off error. In practice, however, that is prohibitively expensive for large grids, and stopping criteria [26] are more typically set for residuals of ~ 10^{-5} to 10^{-6} .

2.3 EULAG Simulation of Gravity Waves

The advection of potential temperature *perturbation* and the treatment of the convective derivative of the environmental state as an implicit forcing on the rhs of the entropy equation (3) has significant benefits for computational stability and accuracy. These two features allow stable integration of the terms responsible for gravity-wave propagation, allow conservation of entropy perturbations with accuracy to round-off error, and obviate changes in environmental stratification due to numerical error. Historically, these features were developed for high quality mesoscale gravity wave simulations in precursor models to EULAG. They are among the key ingrediants of EULAG's multi-scale capability. A more complete development of EULAG's advanced features is given in [1].

3 LOCALIZED INTERNAL WAVES IN HELD SUAREZ SIMULATIONS

Held and Suarez [6] describe an idealized climate test for testing the dry dynamic core (dycore) of climate models. They prescribe idealized environmental profiles, and employ Rayleigh damping of low level winds and Newtonian relaxation of the temperature to replace complicated surface exchanges, as well as radiative and moist physics. In spite of this simplicity, the Held–Suarez (HS) climate develops into an approximately stationary, quasi-geostrophic state that replicates many of the essential features of the Earth's climate, such as the mean meridional circulation, equatorial easterlies, the westerly midlatitude zonal jets, and fronts.

Idealized HS simulations were run with three different horizontal grid resolutions, from an initial no-flow state to an approximately quasi-geostrophic one for which statistics are stationary. Typically this requires ~ 240 days of integration, although by ~120 days the general morphology of the quasi-geostrophic state is established. Table 1 summarizes the three simulations.

Grid size and resolution refer only to the horizontal dimension; all three simulations used the same vertical grid with 41 vertical nodes, a domain depth of 30 km, and a vertical stretching using an analytically specified, stationary exponential mapping (scale height = 13.2 km) that concentrated vertical levels at lower atitudes such that Δz = 300 and 2590 m at the domain bottom and top, respectively. In accord with Section 2.1, the transformed coordinates used a uniform vertical increment of $\Delta \bar{z}$ = 750 m. CPU time per day refers to the total CPU time over all processors (PEs) on Bassi, a POWER 5+ IBM RS/6000 at NERSC. EULAG scales very well up to thousands of PEs, but an upper limit for good scaling varies according to grid size [1]. In particular the HS2 grid

will work well with up to 512 PEs, but queuing times on Bassi dictated 128 PEs for better throughput. The HS1 and HS0 grids were run using 64 and 16 PE's, respectively. The CPU times given are for integrations in the quasi-geostrophic regime. Early in the spinup, the CPU times are much less.

Simulation	Grid Size	Resolution	Integration Interval	CPU Time per Day
HS0	128 x 64	2.813^{o}	300 d	0.3 hr
HS1	256 x 128	1.406^{o}	300 d	3.6 hr
HS2	512 x 256	0.703^{o}	120 d	100 hr

Table 1: Summary of Held-Suarez simulations

3.1 Global Character of the Held-Suarez Quasi-geostrophic State

The quasi-geostrophic regime of Held-Suarez flows shows striking synoptic-length filaments in the surface potential temperature field, sweeping west to east around the planet. They arise from large horizontal gradients of potential temperature – animations of which are strikingly reminiscent of satellite imagery of frontal motions. Figure 1 shows that front thickness decreases dramatically with increasing grid resolution, attesting to the quality of EULAG's NFT numerics in resolving fine scale features. Figure 2 (left panel) shows their appearance in the intermediate resolution result. Figure 3 depicts the potential temperature (left panel) and zonal wind (right panel) fields at 15km altitude corresponding to Figure 2. At this altitude, the left panel shows that resolution limited, horizontal gradients of potential temperature associated with fronts near the surface generally do not exist (nor at 7.5 km – not shown). The right panel clearly shows the instantaneous, undulating structure of the mid-latitude jet, with maximum jet speeds strongly correlated with maximum horizontal gradients of potential temperature.

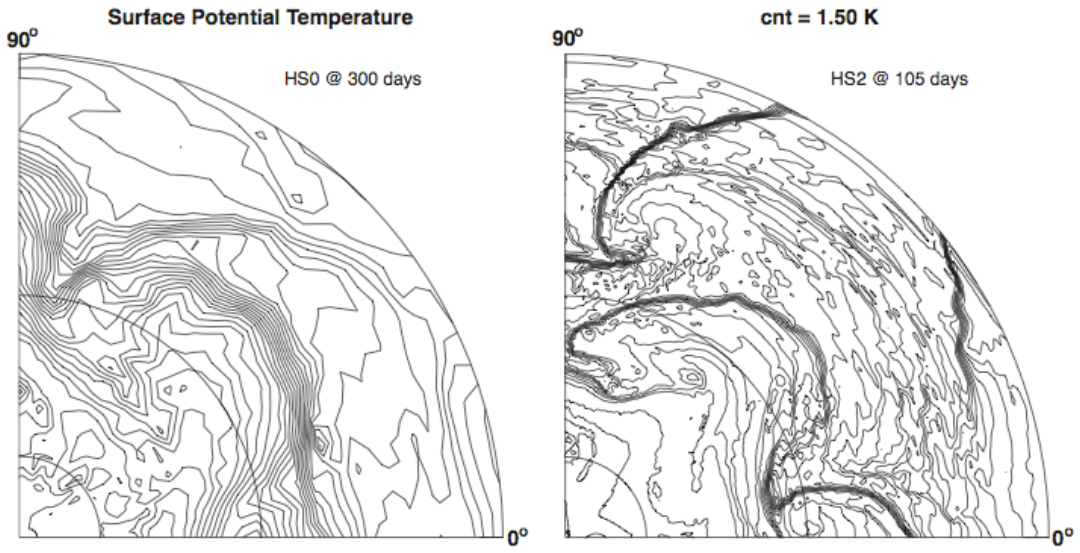

Figure 1: Effect of grid size on the resolution on quasi-geostrophic regime fronts in Held-Suarez simulations. North polar projection. Outermost circle is the equator, also shown are 45^{o} and 75^{o} latitude circles. Left panel: low resolution result (2.8^{o}). Right panel: high resolution result (0.7^{o}).

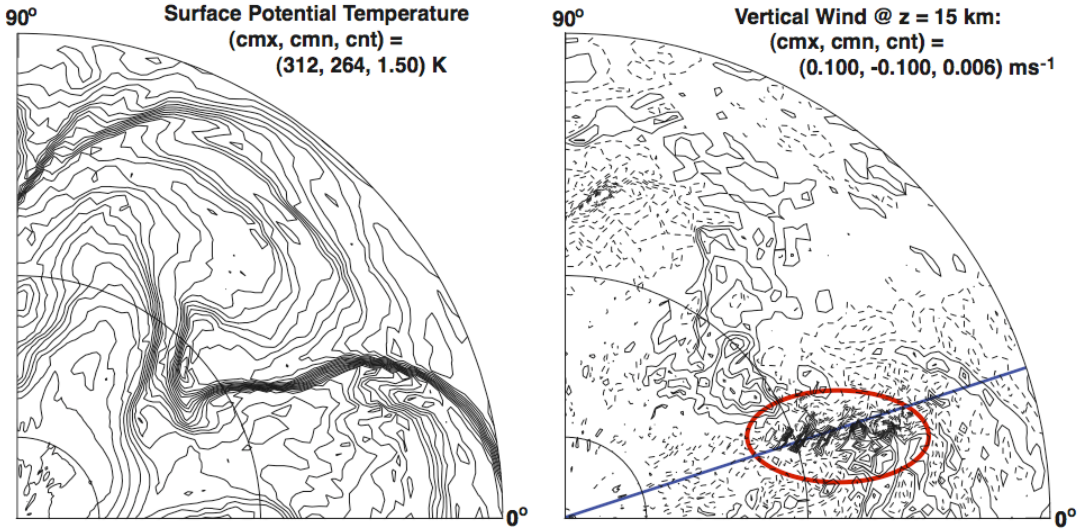

Figure 2: Similar to Figure 1 except for HS1 simulation (1.4° resolution) at 277.50 days. Left panel: surface potential temperature. Right panel: Lower stratosphere vertical wind field depicting localized gravity wave packet (NW5) generated following passage of the front.

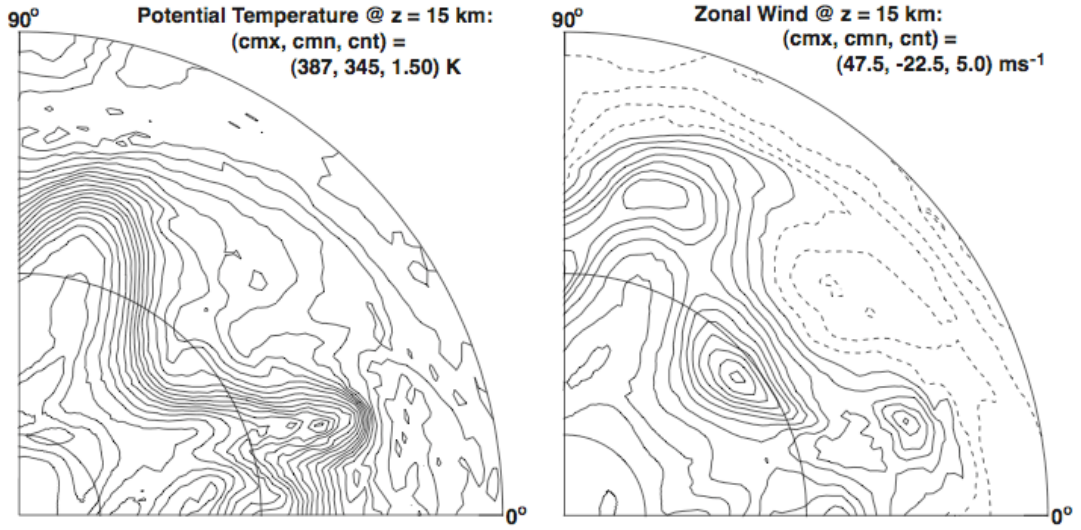

Figure 3: Similar to Figure 2 except potential temperature and zonal winds at 15 km altitude at 277.75 days are shown for simulation HS1.

3.2 Local Wave Event NW5 and its Synoptic Environment

In [23], we reported on the generation of topographically forced internal gravity waves in global simulations with EULAG. Here, we report on the generation of internal gravity waves via frontal collapse. The right panel of Figure 2 depicts a localized wave event, named NW5, that forms briefly following the passage of the front shown in the left panel. The front is moving east (upward in the left panel). The gravity wave packet, by contrast, is very slowly drifting ~ ENE (upwards and slightly to the left in right panel of Figure 2). These events are not observable in the troposphere at 7.5 km altitude, but are obvious at 15 km. Due to their transient nature and short duration, animations of the vertical wind fields were key to their (surprizing) discovery. In the HS1 simulation, ~ 3 to 5 small-scale (i.e., wavelengths less than synoptic) wave packets are observed to form in each hemisphere per week at mid-latitudes in the quasi-geostrophic regime. The

wave packets are localized, with horizontal scales ~ 1000 - 2500 km and time scales of ~1- 2 days.

Wave packet NW5 appears a few hours before day 277.0, and vanishes a few hours after day 278.0 – a lifetime of ~ 30 hrs. The initial development of the waves follows the development of a NS low-pressure ridge that advances from the north to the south. This development coincides with the projection to the south of cooler potential temperatures near 20^o longitude, shown in the left panel of Figure 3; and the breakup and southward ejection of a parcel of high zonal winds from the jet core – observable in the right panel of Figure 3. These two panels also show in the immediate neighborhood of NW5 that the lower stratospheric potential temperature and zonal wind are approximately uniform. Not shown, the meridional wind has an ~ zero NS gradient in the vicinity of NW5, but has a (synoptically) large EW gradient of ~ - 4 x 10^{-5} s^{-1} with NW5 being close to the phase line of zero meridional velocity. Animations show that the synoptic structure is zonally stationary in the vicinity of NW5, beginning at ~ 274.0 days and resuming ~ 276.5 days just as the NW5 event begins.

3.3 Analysis of Wave Event NW5

A more in depth diagnosis of NW5 was undertaken in order to determine if it satisfied a free internal wave dispersion equation, and to determine in particular, what role (i) coriolis force, and/or (ii) nonhydrostatic effects played. The polar projections shown in Figures 1-3, along with similar information from YZ projections depicted in Figures 4-5, were used to estimate the characteristics of the internal waves of NW5. The plane of the YZ slices is depicted by the blue line in the right panel of Figure 2. Wave event NW5 was selected out of approximately two dozen candidates in the interval from 270 – 300 days because it showed the most intense and compact series of waves. There were a number of wave events that were more intense, but occurred over larger spatial and temporal scales and obviously exhibited significant coriolis effects.

The relevant dispersion equation [27] for classical linear inertio -gravity waves is:

$$\omega_{rel}^2 = (\omega - Uk - Vl)^2 = f^2 + N^2(k^2 + l^2)/(m^2 + 1/4H_\rho^2) \qquad (6)$$

Here, ω, f, and N represent wave frequency, local coriolis parameter, and the local value of Brunt-Vaisala (BV) frequency, respectively. The wavenumbers k, l, and m refer to the zonal, meridional, and vertical directions, respectively. Mean zonal and merdional

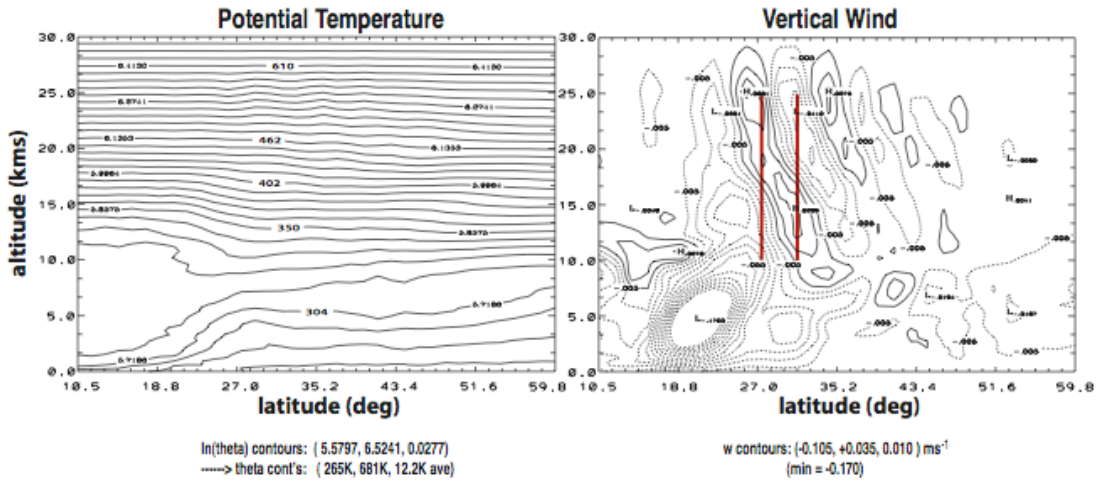

Figure 4: Region containing event NW5 at time 277.75 days. YZ slices at 18.3^o longitude (zonal node i=14, meridional nodes j ∈ [72, 107]). Left panel: potential temperature. Right panel: vertical wind field.

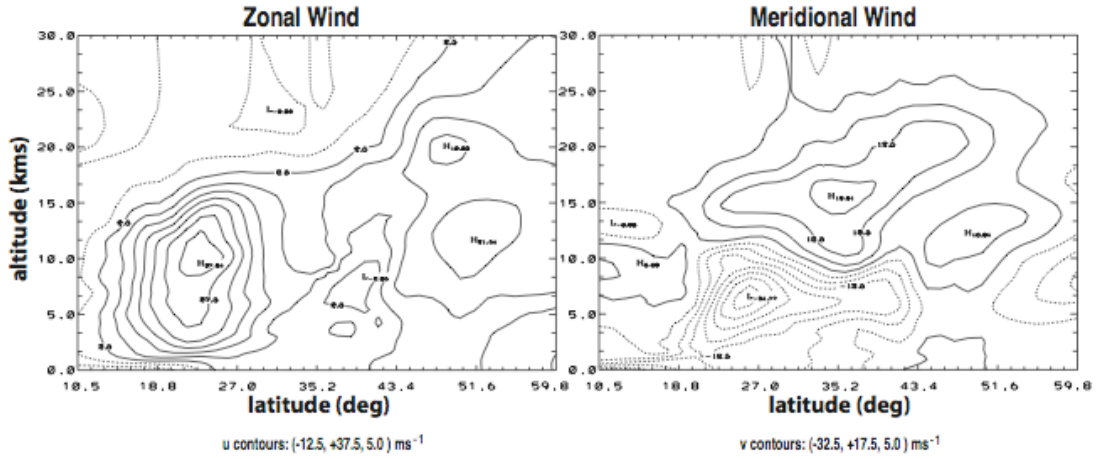

Figure 5: Same as Figure 4 but horizontal winds.

winds, U and V, respectively, are assumed. We use $N = \sqrt{g/H_\theta}$ to estimate the BV frequency, where H_θ is the local potential temperature scale height. The local density scale height is denoted by H_ρ, and is determined from the anelastic basic state profiles. We regard all of these properties with the exception of ω as input parameters, readily estimated from the model solution. The evaluation of the RHS of Eq. (6) then provides the relative frequency, ω_{rel}. Given the estimated wavenumbers and mean wind speeds, the relative frequency then provides the absolute frequency. Checks for consistency are provided by independently estimating the wave phase speeds and/or period from the model solution. Since event NW5 is distributed over a region of space and time, and the local synoptic environment is changing as the wave packet evolves, this diagnosis cannot be expected to provide a precise match to Eq. (6). It has already been noted that the zonal shear of meridional wind is not negligible. Nevertheless, we have found a reasonably good match occurs if wave properties near the center (in time and space) of the event are used. Mean values are listed in Table 2, along with estimates of standard deviation when available.

Using the values listed in Table 2, it is readily estimated that the relative frequency is $\omega_{rel} = 2\pi/2.4$ hr^{-1}. Substituting in the mean wind speeds, then the absolute frequency that

Wave Property	Symbol	Est. mean	Est. SD
zonal wavelength	λ_x	430 km	50 km
meridional wavelength	λ_y	610 km	50 km
vertical wavelength	λ_z	14.0 km	0.5 km
zonal phase speed	c_x	-22 ms^{-1}	
meridional phase speed	c_y	-31 ms^{-1}	5 ms^{-1}
period	P	5.0 hr	
potential temperature scale height	H_θ	27.5 km	
BV frequency	N	0.019 s^{-1}	
zonal wind	U	10 ms^{-1}	5 ms^{-1}
meridional wind	V	20 ms^{-1}	5 ms^{-1}

Table 2: Summary of NW5 properties.

results is ω = -2π/4.5 hr^{-1}, a good match to the observed period listed in Table 2. Note that the negative root from Eq. (6) is choosen. This is required because the phase speeds are negative. Next we compute the phase speeds, $c_x = \omega/k$ and $c_y = \omega/l$. The results are -38 and -27 ms^{-1}, respectively. The magnitudes are 20% too large, but given the uncertainties in Table 2 as well as the constant wind assumption, we believe the result provides an acceptable confirmation of wave event NW5 physics.

A few more observations are possible. Comparing terms in Eq. (6), it immediately follows that coriolis accerleration is negligible since $(f/\omega_{rel})^2$ = 0.010 – thus NW5 consists of pure internal gravity waves. The density stratification effect on the waves is larger but still small as $(1/4H_\rho^2)/m^2$ = 0.050. An estimate of nonhydrostatic effect can also be made according to $n_{hydro} = 1 + (\partial p_{phy}/\partial z)/(\rho g)$, where ρ is the basic state density, z is the physical altitude, and p_{phy} is the *recovered* physical pressure (see [3] for details). A hydrostatic state corresponds to $n_{hydro} = 0$. This metric has been computed along the two vertical paths shown by the red lines in the right panel of Figure 4 in order to improve the signal to noise ratio. The result is Δn_{hydro} = 0.04.

4 GLOBAL SIMULATIONS OF BAROCLINIC INSTABILITY

Jablonowski and Williamson [5] describe a dycore test specifically taylored to illuminate model behavior on baroclinic modes – extremely important in climate simulations. They prescribe environmental states for zonal wind, temperature, and geopotential (gradient of gravity) in eta coordinates (a normalized pressure). This state is in geostrophic and hydrostatic balance. A guassian perturbation is applied to the zonal wind to excite baroclinic instability. The simulation consists of following the nascent linear growth of the instability and briefly, the following period of baroclinic wavebreaking.

4.1 Balanced States in EULAG

The Jablonowski and Williamson (JW) test was designed with hydrostatic models in mind. EULAG is nonhydrostatic, uses potential temperature rather than temperature, and geometric height rather than eta coordinates. In principle, this requires the inversion of the geopotential to set up the corresponding environmental state. Fundamentally, however, the governing equations of EULAG are not those of the dycores in [5], thus even if the geopotential is inverted to machine precision, the resulting environmental field will *not be balanced* for EULAG.

Significant effects from neglecting this factor are implied in [18] in a study on baroclinic waves simulated by EULAG with its default anelastic model and a recent variant based upon the psuedo-incompressible model of [28]. Thus in practice, we specify eta as a function of altitude *a priori*, employ the specified environmental temperature and compute the environmental potential temperature, and correct the zonal wind so that an initialization consistent with a balanced state of EULAG's equations is obtained. Without the zonal wind perturbation, the model solution then remains balanced for ~ 20 days of integration.

The zonal wind correction required for balance is small, but not negligible. It increases the jet core speeds ~5%, compared to [5]. We have partially compensated for this effect by modifying the wind speed parameter, u00 (see Table 3), such that after geostrophic adjustment, the core wind speed matches the JW specification of 35 ms^{-1} to within ± 0.01 ms^{-1} during the first 5 days of simulation. This compensation does not correct subtle differences in gradients of the environmental zonal wind.

4.2 Grid Convergence

Baroclinic instability simulations were run using the same three horizontal grid resolutions as for the HS simulations, see Table 3. Similarly, all three simulations used the same vertical grid, only now with 47 vertical nodes, a domain depth of 23 km, and uniform vertical increments. CPU times per day on Bassi were comparable to those found in the HS simulations. The times listed in Table 3 are for the planetary wave breaking regime. For a given level of convergence of the Krylov solver, CPU times can be much less during the linear growth phase. However, this was generally offset by the result that convergence generally had to be increased with grid size in order to maintain a high level of accuracy. Due to the shorter integration times for the baroclinic vs HS simulations, throughput was improved by using smaller numbers of PE's for the two larger grids. Simulations BA0, BA1, and BA2 used 16, 32, and 64PE's, respectively.

Simulation	Grid Size	Resolution	Integration Interval	CPU Time per Day	u00
BA0	128 x 64	2.813^o	20 d	0.3 hr	33.38 ms^{-1}
BA1	256 x 128	1.406^o	20 d	6.0 hr	33.26 ms^{-1}
BA2	512 x 256	0.703^o	16 d	100 hr	33.23 ms^{-1}

Table 3: Summary of Baroclinic Instability Simulations

Figure 6 shows 10 hPa contours of surface pressure at 8 days, relative to the mean surface pressure of 101 kPa, for the three grid sizes. It clearly indicates that simulations BA1 and BA2 are closer to each other than are BA1 and BA0 or BA2 and BA0. Not shown, the level of grid convergence at 6 days between BA1 and BA0 is similar to that between BA2 and BA1 shown in Figure 6. At 8 days, the approximate end of the linear growth regime, only the core of the wave packet is similarly represented with all three grid resolutions. The trailing and leading edges of the wave packet show more notable differences – which continue to increase as the flow develops into the baroclinic wave breaking regime. The locations and amplitudes of the extreme surface pressure features are given in Table 4 for all three resolutions to facilitate quantitative comparison.

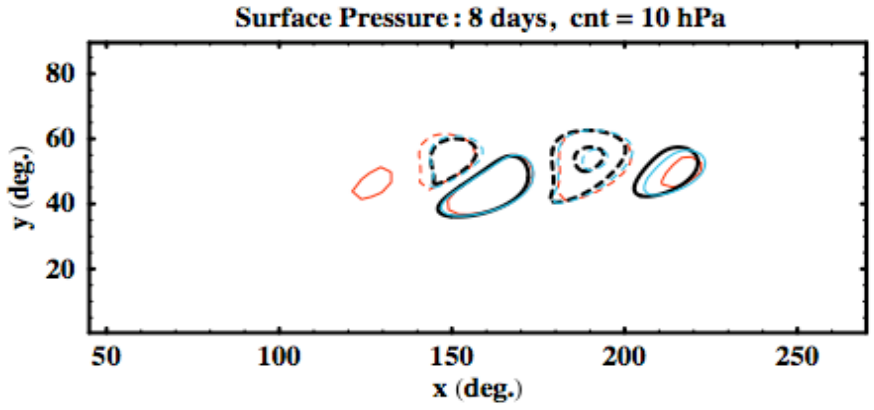

Figure 6: Grid convergence at 8 days. Rectangular XY plots of surface pressure, p. Dashed contours are for p < 101 kPa, solid contours are for p > 101 kPa. Red, green, and dark blue contours correspond to simulations BA0, BA1, and BA2, respectively. Contours shown are ± 5 and -15 hPa.

Figure 7 shows grid convergence at 11 and 16 days. At 11 days, the flow is well into the wavebreaking regime, although some linear features still remain at the leading edge

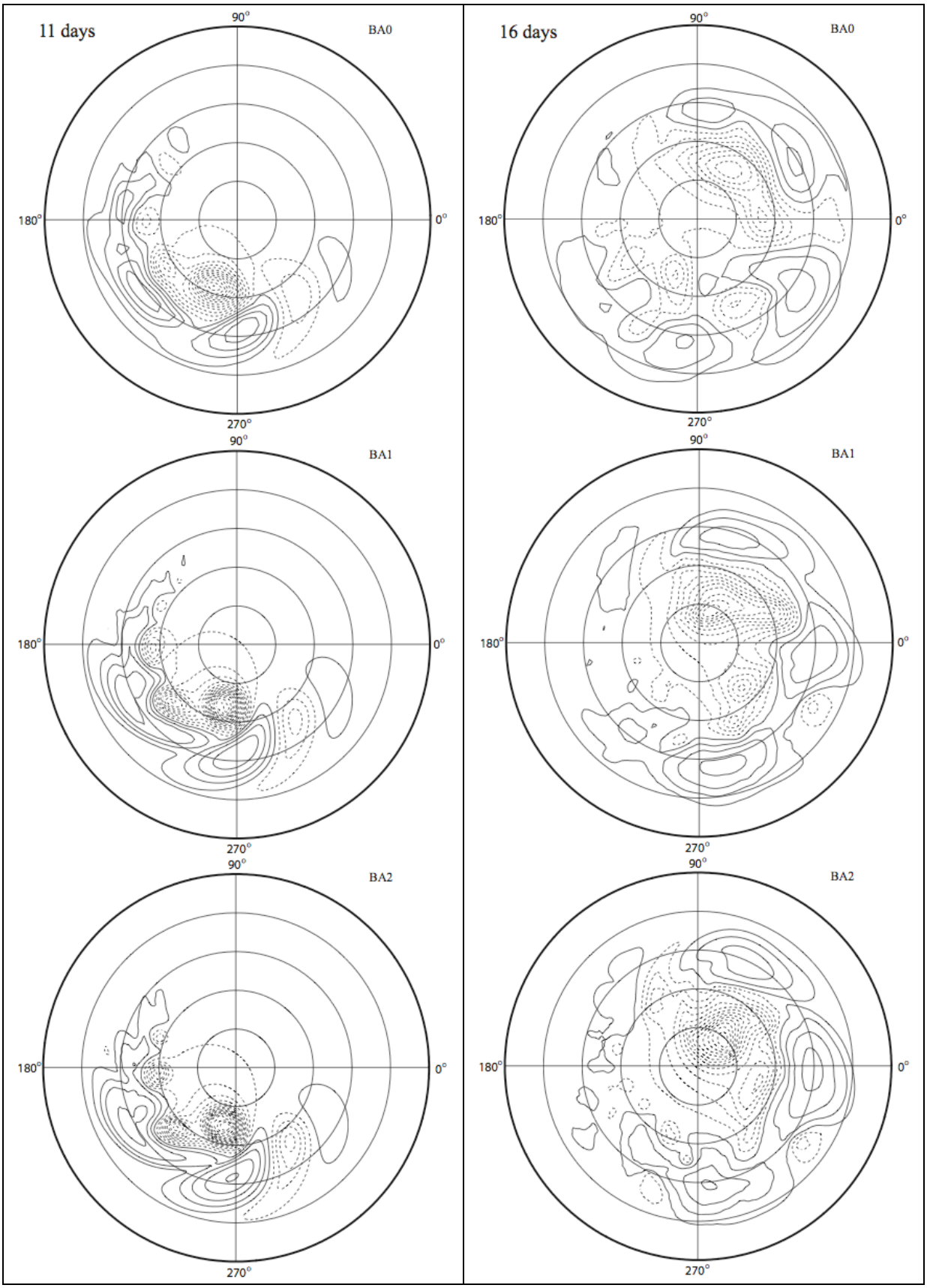

Figure 7: Grid convergence at 11 and 16 days via surface pressure diagnostic. North polar projections, latitude circles every 15° from 15° N (bold) to 75°N (smallest). Solid contours are for p > 101 kPa, dashed contours are for p < 101 kPa. Contour increment is 5 hPa for left panels (11 days) and 10 hPa for right panels (16.0 days). Horizontal resolutions: BA0 (2.8°), BA1 (1.4°), BA2 (0.7°). See Table 4 for extrema.

Day	Sim.	Ext.	λ (deg)	ϕ (deg)	Amp. (hPa)	Δλ (deg)	Δϕ (deg)	Δs (km)	Δamp (hPa)
4	BA0	H1	82	46.	1.	-3.	1.	260	0.
		L1	106.5	47.	-1.	0.5	-0.5	65	0.
	JW	**H1**	**85.**	**45.**	**1.**	*	*	*	*
		L1	**107.**	**47.5**	**-1.**	*	*	*	*
6	BA0	H1	121.	45.5	4.	-4.	-0.5	315	0.
		L1	147.5	49.	-4.	0.5	-0.5	65	4.
	JW	**H1**	**125.**	**46.**	**4.**	*	*	*	*
		L1	**147.**	**49.5**	**-8.**	*	*	*	*
8	BA0	H1	161.	45.5	10.	-0.5	0.	40 (235)	0.
		L1	190.	52.5	-12.5	0.	2.5	280 (570)	6.
	BA1	H1	162.	46.5	10.	0.5	1.	115	0.
		L1	191.	55.	-16.	1.	0.	65	2.5
	BA2	**H1**	**161.5**	**45.5**	**10.**	*	*	*	*
		L1	**190.**	**55.**	**-18.5**	*	*	*	*
	JW	H1	164.	45.5	10.	2.5	0.	195	0.
		L1	192.	57.5	-30.	2.	2.5	305	-11.5
11	BA0	H1	273.5	47.5	20.	5.5	0.	410	-2.5
		L1	251.	63.	-62.5	-8.5	-4.	600	20.
	BA1	H1	271.	48.0	20.	3.	0.5	230	-2.5
		L1	259.5	65.5	-72.5	0.	-1.5	165	10.
	BA2	**H1**	**268.**	**47.5**	**22.5**	*	*	*	*
		L1	**259.5**	**67.**	**-82.5**	*	*	*	*
	JW	H1	262.5	45.5	30.	-5.5	-2.	480	7.5
		L1	254.	68.5	-75.	-5.5	1.5	285	7.5
16	BA0	H1	325.	42.5	27.5	-31.5	-3.5	2520	-10.
		L1	56.	67.	-70.	9.5	-9.	1050	62.5
	BA1	H1	354.	44.	32.5	-2.5	-2.	295	-5.
		L1	71.	77.5	-102.5	24.5	1.5	640	30.
	BA2	**H1**	**356.5**	**46.0**	**37.5**	*	*	*	*
		L1	**46.5**	**76.0**	**-132.5**	*	*	*	*
	JW	H1	337.5	43.	40.	-19.	-3.	1540	2.5
		L1	36.	72.	-115	-10.5	15.	550	17.5

Table 4: Baroclinic Instability Simulations – Surface Pressure Extrema. JW refers to Eulerian-spectral dycore of [JW06]. Sim., Ext., and Amp. refer to simulation, pressure extremum, and amplitude of extrema relative to mean surface pressure, respectively. H1 and L1 refer to maximum pressure high and minimum pressure low. Longitude and latitude are denoted by λ and ϕ, respectively. Δ quantities denote differences from reference simulation **in bold**. Δs denotes distance (on the sphere) of extrema center from corresponding location in reference simulation (values in parentheses are referenced to JW). Estimated errors are 1^{o} in latitude and 100 km in longitude, and 1/1.25/2.5 hPa in amplitude for days 4,6/8/11,16 respectively.

of the wave packet which is nearing completion of a global circuit. At the trailing edge, a wake has developed. The lows have moved northward and intensified vs. the highs that have remained close to 40^o N – the latitude of the incipient perturbation. Also of interest is that flow over the pole is becoming significant. Prior to this time, the quality of polar boundary conditions is of little consequence. At 16 days, no obvious linear features remain, a strong polar low has formed, and a broader nearly uniform pressure (~ 101 kPa) wake has formed. Table 4 also contains data for all three resolu-tions at these two times.

Careful inspection of the figures and tabulated data at 11 and 16 days again indicates that simulations BA1 and BA2 are, *in toto*, closer to each other than are BA1 and BA0 or BA2 and BA0. While this indicates reasonable grid convergence for most features, the possibility of nonhydrostatic effects beginning to be felt at the highest resolution should be considered. In particular, note that the strong polar low in the BA2 result at 16 days is centered at ~75^o N, where the local zonal resolution is ~20 kms. This is close to the threshold (~10 km, [23] and [29]) at which nonhydrostatic effects become significant. This effect *could* be related to the apparent non-converging trend in the amplitude of the low (-70, -102.5, and -132.5 hPa for BA0, BA1, and BA2, respectively), but clearly a more definitive diagnoses of nonhydrostatic effect vs. grid size is needed.

4.3 Comparison with JW 2006

EULAG's linear regime results at days 4, 6, and 8 (Figure 6) were compared against the surface pressure plots on the left side of Figure 5 of [5]. To facilitate comparison, we carefully estimated the locations and amplitudes of the pressure extrema shown in JW's Figure 5 and recorded those estimates in Table 4. The corresponding values for EULAG are also entered. Since grid convergence is assured for the core of the wave packet at this time (see preceding section), there is no need to examine the BA1 and BA2 results at 4 and 6 days. The data in Table 4 indicate an initial difference in location of the extreme high pressure, H1, of 260 km. The difference in the location of the extreme low pressure, L1, is zero to within accuracy of measurement. Averaged over 4 days, the 260 km displacement of H1 corresponds to a phase speed difference of 0.8 ms^{-1}, with EULAG being slower. From 4 to 6 days, the distances between the EULAG and FV extrema remain the same, implying they have the same phase speeds to within the accuracy of the measurement, which for 2 days is 0.4 ms^{-1}. We observe that the match in positions of L1 up to day 6 corresponds to a maximum phase speed difference of 0.1 ms^{-1}. These differences are small compared to the baroclinic wave speed, which averages 20 ms^{-1} from 4 to 8 days. These trends continue to 8 days, with the exception that the amplitude of L1 grows more rapidly for the FV result than is seen in any of the EULAG results.

Since [18] and [16] both indicate that the anelastic model should propagate deep baroclinic modes too quickly[1], and the above results indicate EULAG's phase speeds are at most, too slow, we can conclude that deep baroclinic modes are of little consequence during the linear growth phase of the test problem. The results from [18] also predict that the anelastic model will grow baroclinic disturbances more slowly. This fits in with the observed results for L1 at 6 and 8 days; but conflicts with the good match of high pressure amplitude.

[1]Although the computational results from [18] support the *trends* predicted by [16], the magnitudes of the effects are less than predicted by the normal mode analysis. In particular, the excess wave speed of the deep baroclinic wave mode of the anelastic model vs. the psuedo-incompressible model is ~3%.

We conclude this section with a comparison of the wavebreaking regime results. The reader is referred to the top row of Figure 9 (the Eulerian-spectral dycore results) of [5]. These results are at T170 spectral resolution, comparable to the BA2 results (0.70^o horizontal resolution) in our Figure 7. JW's results use a stereographic projection whereas the EULAG results shown in Figure 7 use a polar projection. Provided one takes care to match up the latitudes of various features on the two types of projections (the polar projection has uniform latitudinal increment whereas the stereographic has larger increments at lower latitude[2]) visual comparison can be made. All panels in Figure 9 of [5] use a contour interval of 5 hPa, whereas in our Figure 7 only the 11 day results use this interval and the 16 days results use 10 hPa. Further, the contours in JW's figures are indexed to the reference pressure of 100 kPa, whereas those in Figure 7 straddle the reference pressure (e.g, they begin at ± 2.5, 5 hPa). Locations and amplitudes of the JW pressure extrema at 11 and 16 days are in Table 4.

At 11 days, there remains general agreement between JW and EULAG in the global structure of the solution. The two most notable differences are in details of the wake developing at the trailing edge of the wave packet, and in the appearance of a high pressure ridge connecting the two strongest highs in the EULAG results. Due to these two global features, it appears that BA0, BA1, and BA2 are converging to a solution that is *not quite* the same as that given in JW. This does not appear to be the case during the linear growth regime. The amplitude of H1 is 22.5 hPa in BA2 vs. 30 hPa for JW. The amplitudes of L1 compare more favorably, -82.5 and -75 hPa for BA2 and JW, respectively. The zonal locations of H1 and L1 are advanced 5.5^o and -5.5^o, respectively, for BA2 vs. JW. However L1 is now at 68^oN so the actual physical displacement between the BA2 and JW locations for L1 is similar in magnitude to that at 8 days (~300 km). H1, however remains in the mid-latitudes and shows ~ 2X the displacement compared to 8 days. Because phases of various highs and lows are advanced or retarded, BA2 vs. JW; and amplitudes may be less or more, it is hard to conclude at this time that differences are due to limitations of the anelastic model or other effects such as numerics [2], filtering, nonhydrostatics, initialization, environment, and so forth.

The comparison between BA2 and JW at 16 days gives very similar results to those at 11 days. There still remains general agreement between the two results in the global structure of the solution, although it is weaker than at 11 days. Again, two of the most notable differences are in details of the trailing wake region, and in the appearance of ridges connecting high pressure regions. There are more obvious differences in the locations and amplitudes of some of the sub-extrema (lows and highs other than H1 and L1). That BA0, BA1, and BA2 are converging to a solution that is not quite the same as that given in JW is more apparent. BA2's extrema show greater displacements (compared to 11 days) relative to JW of 1540 (19^o) and 550 (4^o) kms (degrees zonally), for H1 and L1, respectively. The amplitudes of H1 are 37.5 hPa and 40 hPa, for BA2 and JW, respectively – a better match that at 11 days. The amplitudes of L1 are -132.5 hPa and -115 hPa for BA2 and JW, respectively. Interpretations of these differences remain as for the comparison at 11 days.

5 SUMMARY AND REMARKS

Held Suarez simulations with EULAG clearly indicate that the model is capable of resolving small scale internal waves due to frontal collapse that are only a few grid intervals in wavelength. This mechanism complements previously reported [23] topo-

[2]The stereographic projections in Figure 9 of [5] start at 15^o N latitude, and index other latitude circles every 15^o northward to 75^o (private comm. with C. Jablonowski).

graphical generation of internal waves in EULAG global simulations. These waves appear to reasonably satisfy classical dispersion relations for such waves. In the presently diagnosed case, which occurred for the intermediate resolution grid (1.4^o), the waves were sufficiently small that coriolis accelerations were negligible and the waves behaved as pure internal gravity waves. We note that a number of wave events characterized by somewhat larger scales were also evident, and these clearly showed the signatures of inertio-gravity waves. In fact there appear to be a continous spectrum of waves, from small internal gravity waves to planetary scale. Future investigations will examine the role of grid resolution in producing these waves, and in resolving nonhdrostatic effects well enough that it begins to alter synoptic flow. We conjecture that the HS1 resolution is close to the threshold for capturing pure interval waves, and that the success of EULAG in resolving them may stem from its numerical design [1] as well as from the correct asymptotic behavior of the anelastic model in capturing mulitscale interactions [19].

The baroclinic instability study failed to reveal pathologies predicted for the anelastic model in [16]. During the linear growth phase, which is the only time during this test case that phase speeds can be compared with high accuracy, differences between anelastic EULAG and hydrostatic JW dycore results is negligible. Apparently the deep baroclinic modes – which the modal analysis indicates will be propagated too quickly by an anelastic model – are of little consequence during this phase of the test case. During the baroclinic wavebreaking phase of the test, differences between EULAG simulations and those of JW emerge, but are more in the nature of details of particular features, with good agreement in the overall global structure of the flow as well in numerous other particular features. Nevertheless, it does become clear by 16 days, as judged from a grid convergence study, that the EULAG solution is not quite the same as the Eulerian-spectral dycore solution of JW. Because phases of various highs and lows are advanced or retarded, and amplitudes may be less or more in the EULAG simulation BA2 vs. JW; it is impossible to conclude that limitations due to use of the anelastic model are present in the wavebreaking regime. Other effects such as numerics [2], filtering, nonhydrostatics (recall from the grid convergence study that the zonal resolution of the extreme low pressure at 16 days is ~20 km), initialization, environment, and so forth may overwhelm any errors in representing deep modes. Future extensions of the present study will attempt to examine these effects in detail. In particular, the pseudo-compressible variant of EULAG may allow a sharpened assessment of deep baroclinic modes while keeping other factors nearly the same.

6 ACKNOWLEDGEMENTS

The Authors wish to express their thanks to P.K. Smolarkiewicz for invaluable help in setting up EULAG to do the baroclinic instability test. This research was supported by the Office of Science (BER), U. S. Department of Energy.

REFERENCES

[1] J.M. Prusa, P.K. Smolarkiewicz, and A.A. Wyszogrodzki. EULAG: a computational model for multi-scale flows. *J. Computers and Fluids.* **37** , pp. 1193–1207 (2008).

[2] P.K. Smolarkiewicz, L.G. Margolin, and A.A. Wyszogrodzki. A class of nonhydrostatic global models. *J. Atmos. Sci.* 58, pp. 349-364 (2001).

[3] B.J. Abiodun, J.M. Prusa, and W.J. Gutowski. Implementation of a non-hydrostatic, adaptive-grid dynamics core in CAM3. Part I: Comparison of dynamics cores in aqua-planet simulations. *Clim. Dynamics*. 31, pp. 795-810 (2008).

[4] B.J. Abiodun, W.J. Gutowsk, and J.M. Prusa. Implementation of a non-hydrostatic, adaptive-grid dynamics core in CAM3. Part II: Dynamical influences on ITCZ behavior and tropical precipitation. *Clim. Dynamics*. 31, pp. 811-822 (2008).

[5] C. Jablonowski and D.L. Williamson, A baroclinic instability test case for atmospheric model dynamical cores. *Q. J. R. Meteorol. Soc*. **132,** pp. 2943-2975 (2006)

[6] I.M. Held and M.J. Suarez. A proposal for intercomparison of the dynamical cores of atmospheric general circulation models. *Bull. Amer. Meteor. Soc.* **75**, pp. 1825-1830 (1994).

[7] L.G. Margolin and W.J. Rider. A rationale for implicit turbulence modeling, Int. J. *Numer. Meth. Fluids* **39**, pp. 821-841 (2002).

[8] L.G. Margolin, W.J. Rider, and F.F. Grinstein FF. Modeling turbulent flow with implicit LES. *J. Turb.* **7**, No.15., DOI: 10.1080/14685240500331595 (2006).

[9] F.B. Lipps and R.S. Hemler. A scale analysis of deep moist convection and some related numerical calculations. *J. Atmos. Sci*. **39**, pp. 2192-2210 (1982).

[10] P.K. Smolarkiewicz and J.M. Prusa. Towards mesh adaptivity for geophysical turbulence: continuous mapping approach. *Int. J. Numer. Meth. Fluids* **47**, pp. 789-801 (2005).

[11] S.M. Polavarapu and W.R. Peltier. The structure and nonlinear evolution of synoptic scale cyclones: life cycle simulations with a cloud-scale model. *J. Atmos. Sci.* **47**, pp. 2645-2673 (1990).

[12] S.R. Lantz and Y. Fan. Anelastic magnetohydrodyanmical equations for modeling solar and stellar convection zones. The Astrophy. J. Supp **121**, pp. 247-264 (1999).

[13] J.R. Elliott and P.K. Smolarkiewicz. Eddy resolving simulations of turbulent solar convection. *Int. J. Numer. Meth. Fluids* **39**, pp. 855-864 (2002).

[14] G.A. Glatzmaier and P.H. Roberts. An anelastic evolutionary geodynamo simulation driven by compositional and thermal convection. *Physica D* **97**, pp. 81-94 (1996a).

[15] G.A. Glatzmaier and P.H. Roberts. Rotation and magnetism of Earth's inner core. *Science* **13**, pp. 1887-1891 (1996b).

[16] T. Davis, A. Staniforth, N. Wood, and J. Thuburn. Validity of anelastic ond other equation sets as inferred from normal-mode analysis. *Q. J. R. Meteorol. Soc.* **129**, pp. 2761-2775 (2003).

[17] P.K. Smolarkiewicz and J. Szmelter. Iterated upwind schemes for gas dynamics. *J. Comput. Phys* **228**, pp. 33-54 (2009).

[18] P.K. Smolarkiewicz and A. Dörnbrack A. Conservative integrals of adiabatic Durran's equations. *Int. J. Numer. Meth. Fluids* **56**, pp. 1513-1519 (2008).

[19] R. Klein, U. Achatz, D. Bresch, O.M. Knio, and P.K. Smolarkiewicz. Regime of validity of sound-proof atmospheric flow models. *J. Atm. Sciences*, submitted (2010).

[20] W.W. Grabowski and P.K. Smolarkiewicz. A multiscale model for meteorological research. *Mon. Wea. Rev*. **130**, pp. 939-956 (2002).

[21] J.M. Prusa and P.K. Smolarkiewicz. An all-scale anelastic model for geophysical flows: dynamic grid deformation. *J. Comput. Phys.* **190**, pp. 601- 622 (2003).

[22] N.P. Wedi and P.K. Smolarkiewicz. Extending Gal-Chen & Somerville terrain – following coordinate transformation on time-dependent curvilinear boundaries. *J. Comput. Phys.* **193**, pp.1- 20 (2004).

[23] J.M. Prusa and W.J. Gutowski. MPDATA and grid adaptivity in geophysical fluid flow models. *Int. J. Num. Methods in Fluids* **50**, pp. 1207-1228 (2006).

[24] P.K. Smolarkiewicz and J.M. Prusa. Forward-in-time differencing for fluids: simulation of geophysical turbulence. Turbulent Flow Computation, Ch. 8, Eds. D. Drikakis and B.J. Guertz, Kluwer Academic Publishers, pp. 279-312 (2002).

[25] P.K. Smolarkiewicz. Multidimensional positive definite advection transport algorithm: an overview. *Int. J. Numer. Meth. Fluids* **50**, pp. 1123-1144 (2006).

[26] P.K. Smolarkiewicz, V. Grubisic, and L.G. Margolin. On forward-in-time differencing for fluids: stopping critria for iterative solutions of anelastic pressure equations. *Mon. Wea. Rev.* **125**, pp. 647-654 (1997).

[27] D.G. Andrews, J.R. Holton, and C.B. Leovy. Middle Atmosphere Dynamics. Academic Press, Inc., Orlando, FL. Chap. 4, pp. 150-219 (1987).

[28] D.R. Duran. Improving the anelastic approximation. *J. Atmos. Sci.* **46**, pp. 1453-1461 (1989).

[29] N.P. Wedi and P.K. Smolarkiewicz. A framework for testing global non-hydrostatic models. *Q. J. Royal Meterol. Soc.* DOI: 10.1002/qj.377 (2009).